



Hierarchical hollow urchin-like NiCo_2O_4 nanomaterial as electrocatalyst for oxygen evolution reaction in alkaline medium

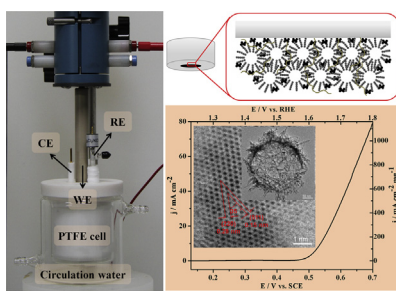
Juan Wang, Tian Qiu, Xu Chen, Yanluo Lu, Wensheng Yang*

State Key Laboratory of Chemical Resource Engineering, Beijing University of Chemical Technology, Beijing 100029, China

HIGHLIGHTS

- Hierarchical hollow urchin-like NiCo_2O_4 (HU- NiCo_2O_4) is facilely synthesized.
- HU- NiCo_2O_4 shows high activity and stability for oxygen evolution reaction.
- High stability of HU- NiCo_2O_4 electrode is due to abundant diffusion paths of gas.

GRAPHICAL ABSTRACT



ARTICLE INFO

Article history:

Received 3 April 2014

Received in revised form

5 June 2014

Accepted 6 June 2014

Available online 16 June 2014

Keywords:

Electrocatalyst

Oxygen evolution reaction

Spinel nickel–cobalt oxide

Hierarchical structure

Hollow structure

ABSTRACT

Hierarchical hollow urchins of NiCo_2O_4 (HU- NiCo_2O_4) were synthesized by a hard templating method followed by thermal decomposition. The structure consists of three levels of hierarchy i.e., zero-dimensional nanoparticle with a diameter of about 6 nm, one-dimensional chain, and three-dimensional hollow urchin, respectively. Nanoparticle aggregates of NiCo_2O_4 (NA- NiCo_2O_4) were also synthesized by the same procedure in the absence of the hard template. Relative to NA- NiCo_2O_4 , HU- NiCo_2O_4 features a well-connected three-dimensional porous structure, which is beneficial for diffusion of oxygen. Consequently, HU- NiCo_2O_4 displayed superior electrocatalytic activity towards oxygen evolution processes with lower overpotential, higher current density, and higher stability than NA- NiCo_2O_4 .

© 2014 Elsevier B.V. All rights reserved.

1. Introduction

With the decrease of fossil fuel reserves and increasing concerns relating to global warming and climate change, the demands for clean and sustainable energy have continued to increase. Oxygen evolution reaction (OER) is an important half reaction involved in many energy conversion and storage processes such as water splitting and rechargeable metal–air batteries. [1–4] To date, IrO_2

and RuO_2 are the most active OER catalysts, operating in acidic and alkaline solutions. [5–9] However, their applications are limited owing to the high cost and scarcity of the precious metals. Therefore, extensive research effort has been devoted to developing highly active, durable, and low-cost alternatives such as perovskites [10,11] and transition metal oxides. [1,12–17] Among the transition metal oxides, NiCo_2O_4 is one of the most promising materials for use in an alkaline medium, owing to its enhanced electrical conductivity and high number of catalytically active sites [15,16,18–21].

The microstructure of a catalyst is known to significantly influence the catalytic activity. [22–25] Various NiCo_2O_4 microstructures

* Corresponding author. Tel.: +86 10 64435271; fax: +86 10 64425385.

E-mail addresses: yangws@mail.buct.edu.cn, yangws_buct@126.com (W. Yang).

for OER processes have been reported such as core–ring, [19] nanowire array, [15,16] aerogel, [18] hierarchical nanorod, [20] and mesoporous nanoplatelet/graphene. [21] Recently, hierarchical hollow structures have attracted great interest because of the intrinsic advantages of building blocks and additional benefits resulting from the secondary architecture. [26–31] Many studies have demonstrated the higher electrocatalytic performance of such hierarchical hollow structures, owing to their distinguished properties over their solid counterparts. [25,32,33] The building blocks at the nanoscale can maintain high catalytic activities. Moreover, the cavity and the pores on the shell are interconnected to form through holes, which enable both the outer and inner surfaces of the catalyst to come into contact with the reactants and shorten diffusion length paths of the evolved gas. However, to our knowledge, studies on hierarchical hollow NiCo_2O_4 as an OER electrocatalyst have not been reported yet.

In this work, we used a hard templating method followed by thermal decomposition to prepare hierarchical hollow urchins of NiCo_2O_4 (HU- NiCo_2O_4). Nanoparticle aggregates of NiCo_2O_4 (NA- NiCo_2O_4) as the control sample was also synthesized using the same procedure however, in the absence of the hard template. The prepared materials were evaluated as electrocatalysts for OER. HU- NiCo_2O_4 exhibited higher OER electrocatalytic activity with lower overpotential, higher current density, and higher stability when compared with NA- NiCo_2O_4 , owing to the unique hierarchical hollow urchin-like structure.

2. Experimental

2.1. Synthesis of polystyrene latex templates

Polystyrene (PS) particles were prepared by dispersion polymerization of styrene according to the reported procedure. [34] Typically, 1.588 g polyvinyl pyrrolidone (K-30, >95.0%, Xilong Chemical Co. Ltd., Guangdong, China) and 0.1694 g $\text{K}_2\text{S}_2\text{O}_8$ (>99.5%, Xilong Chemical Co. Ltd., Guangdong, China) were dissolved in 100 mL ethanol/deionized water (85:15, (v/v)) in a 500-mL round-bottom flask. The mixture was stirred and purged with nitrogen for 20 min, and heated to 70 °C at a heating rate of 4 °C min^{-1} using a temperature-controlled water bath. Then, 17.5 mL styrene (>98%, Tianjin Fuchen Chemical Regent Factory, Tianjin, China) and 0.175 mL divinyl benzene (>98%, Tianjin Fuchen Chemical Regent Factory, Tianjin, China) were added to the solution. The polymerization was performed at 70 °C for 24 h under nitrogen to completion. The resulting latex particles were collected via centrifugation at $4000 \times g$ for 20 min, washed successively with deionized water and ethanol three times, and freeze dried for 24 h. All reagents were used without further purification. The sulfonated-PS particles were prepared by reaction with concentrated sulfuric acid (18.4 mol L^{-1}). Typically, 1.7 g of as-prepared PS particles was dispersed in 60 mL concentrated sulfuric acid, assisted by sonication for 30 min. The mixture was stirred at 40 °C for 5 h. The resulting particles suspension was centrifuged at $4000 \times g$ for 20 min, washed with deionized water and ethanol for three times, respectively, and dried at 50 °C for 10 h.

2.2. Synthesis of HU- NiCo_2O_4 and NA- NiCo_2O_4

HU- NiCo_2O_4 was synthesized using a hard templating method followed by thermal decomposition. $\text{Ni}(\text{NO}_3)_2 \cdot 6\text{H}_2\text{O}$, $\text{Co}(\text{NO}_3)_2 \cdot 6\text{H}_2\text{O}$, and Na_2CO_3 were obtained from Xilong Chemical Co. Ltd. (Guangdong, China), and used without further purification. Typically, 0.2 g of sulfonated-PS particles was dispersed in 30 mL deionized water, assisted by sonication for 30 min. A mixed solution of 20 mL $\text{Ni}(\text{NO}_3)_2$ (0.03 mol L^{-1}) and $\text{Co}(\text{NO}_3)_2$ (0.06 mol L^{-1}) was

then added to the sulfonated-PS particles dispersion, and the resulting mixture was stirred for 2 h and heated to 60 °C at a heating rate of 4 °C min^{-1} . Then, 20 mL Na_2CO_3 (0.099 mol L^{-1}) was slowly added to the mixture and stirred at 60 °C for 24 h. The resulting product was centrifuged at $1000 \times g$ for 10 min, washed with deionized water for five times, and dried at 50 °C for 10 h, and denoted as P-HU- NiCo_2O_4 . P-HU- NiCo_2O_4 was subsequently calcined in air at 400 °C for 6 h at a heating rate of 2 °C min^{-1} to remove the template, generating HU- NiCo_2O_4 . NA- NiCo_2O_4 was synthesized using the same procedure, but in the absence of the template. The precursor of NA- NiCo_2O_4 is referred as P-NA- NiCo_2O_4 .

2.3. Materials characterization

X-ray powder diffraction (XRD) was used to study the crystal structure of the prepared catalysts. Powder diffraction patterns were recorded on a Rigaku XRD diffractometer (Rigaku Co., Japan) using $\text{Cu K}\alpha$ radiation ($\lambda = 0.15406 \text{ nm}$). The data were collected from $2\theta = 5^\circ$ – 80° at a scan rate of 5° min^{-1} . Field-emission scanning electron microscopy (FESEM) was used to investigate the morphology of the catalysts. FESEM images were obtained on a Zeiss Supra 55 field-emission scanning electron microscope (Carl Zeiss Co., Germany), operating at 20 kV. The Brunauer–Emmett–Teller (BET) specific surface areas were obtained from N_2 adsorption–desorption isotherms that were recorded at 77 K (QUADRASORB SI, Quantachrome Instrument Co., USA). High-resolution transmission electron microscopy (HRTEM) was used to investigate the microstructure of the catalysts. HRTEM images were obtained on a JEM-2100F (JEOL Ltd., Japan).

2.4. Electrochemical measurements

Electrochemical measurements were carried out at 298 K on a PARSTAT 2273 electrochemical system (Ametek Co., USA) comprising a three-electrode electrochemical cell. The catalyst ink was prepared from 2.5 mg catalyst (HU- NiCo_2O_4 or NA- NiCo_2O_4), 2.5 mg XC-72, 100 μL Nafion solution (5 wt%, Sigma–Aldrich Co., USA), 250 μL deionized water, and 750 μL isopropanol. After sonication for 1 h, 6 μL catalyst ink was cast onto the surface of a freshly polished rotating glass carbon disk electrode (RDE, 5 mm diameter, 0.19625 cm^2) to form a film with a catalyst loading of $\sim 0.069 \text{ mg cm}^{-2}$. The as-prepared catalyst film was dried at room temperature. The RDE was then mounted on an interchangeable RDE holder (Pine Instruments, USA). Pt wire and saturated calomel electrode (SCE, saturated KCl, 0.2735 V vs. a standard hydrogen electrode (SHE)) were used as counter and reference electrodes, respectively. The electrolyte was 1 mol L^{-1} NaOH (guaranteed reagent, GR, Beijing Chemical Works) solution, and it was further purified by using the following method: NaOH solution and water purification activated carbon were mixed and oscillated for an hour and then stood overnight; then the solution was filtered by using PTFE membrane to get purified electrolyte. Before measurement, the electrolyte was saturated with oxygen by bubbling high-purity O_2 for 30 min and a flow of O_2 was maintained over the electrolyte during measurements.

Cyclic voltammetry (CV) curves were obtained by sweeping the potential at a sweep rate of 5 mV s^{-1} at 25 °C and 1600 rpm. Polarization curves (linear sweep voltammetry, LSV) were obtained by sweeping the potential from 0.13 to 0.7 V vs. SCE (i.e., 1.23–1.8 V vs. RHE), at a sweep rate of 5 mV s^{-1} at 25 °C and 1600 rpm. Tafel plots were assessed using LSV. [6,12] The stability tests were performed in O_2 -saturated 1 mol L^{-1} NaOH at 25 °C by potential cycling between 0.13 and 0.7 V vs. SCE for given number of cycles (400, 800, 1200 cycles). At the end of each cycling, the resulting electrode was used for LSV curve.

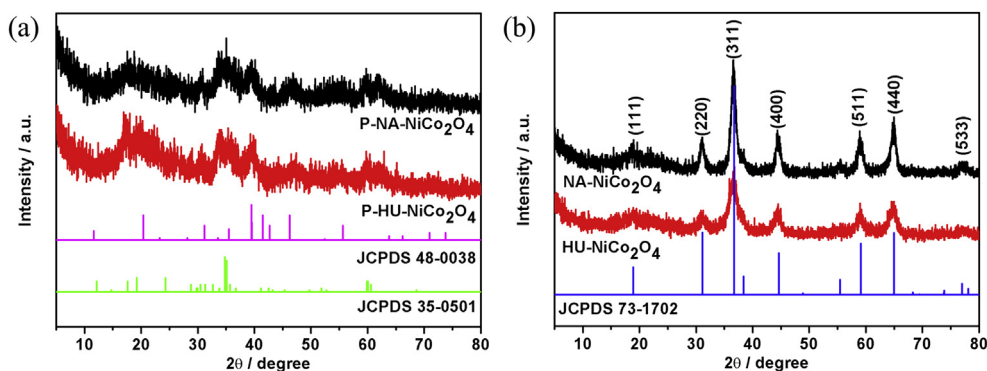
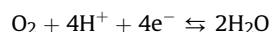


Fig. 1. XRD patterns of (a) P-NA-NiCo₂O₄ and P-HU-NiCo₂O₄, and (b) NA-NiCo₂O₄ and HU-NiCo₂O₄.

The overpotential (η) was calculated using Eq. (1). The equilibrium reaction potential (E^0) of OER was calculated by the Nernst equation (Eq. (2)). And E (vs. reversible hydrogen electrode (RHE)) was calculated using Eq. (3).

$$\eta = E_{\text{applied}} + E_{\text{ref}} - E^0 \quad (1)$$



$$\begin{aligned} E^0 &= E^0 + RT \ln \left\{ \frac{P(\text{O}_2) [\text{H}^+]^4}{P^0} \right\} / nF \\ &= E^0 + 0.05916 \lg [P(\text{O}_2)/P^0] / n - 0.05916 \text{pH} \end{aligned} \quad (2)$$

$$E(\text{vs. RHE}) = E_{\text{applied}} + E_{\text{ref}} + 0.05916 \text{pH} \quad (3)$$

E_{applied} is the applied potential, E_{ref} is the reference electrode potential, E^0 is the standard electrode potential of OER (1.229 V), R is the gas constant ($8.314 \text{ J K}^{-1} \text{ mol}^{-1}$), T is the temperature (298 K), n is the electron transfer number, F is the Faraday constant ($96487 \text{ J V}^{-1} \text{ mol}^{-1}$), $P(\text{O}_2)$ is 0.2 atm when oxygen in the electrolyte is at saturation level, and pH is 14 (electrolyte is 1 mol L^{-1} NaOH). Hence, E^0 was evaluated at 0.3904 V.

3. Results and discussion

3.1. Structure of HU-NiCo₂O₄ and NA-NiCo₂O₄

The bulk crystal structures and morphologies of the two prepared electrocatalysts and their precursors were characterized by XRD, SEM, and HRTEM. As shown in Fig. 1a, P-HU-NiCo₂O₄ and P-NA-NiCo₂O₄ both consist of a mixture of basic cobalt carbonate (JCPDS 48-0038) and basic nickel carbonate (JCPDS 35-0501). The crystallinity of the precursor materials is relatively low. Both P-HU-NiCo₂O₄ and P-NA-NiCo₂O₄ comprises short nanofibers, as observed in Fig. 2. However, the assembly of the short nanofibers in the precursors is different. As shown in Fig. 2c, d, the short nanofibers grow on the surface of the sulfonated-PS particles to form urchin-like P-HU-NiCo₂O₄; in contrast, the short nanofibers grow in a disordered fashion to form P-NA-NiCo₂O₄ (Fig. 2g, h).

After calcination at 400°C , HU-NiCo₂O₄ and NA-NiCo₂O₄ were generated. According to the literature reports, [35,36] the XRD patterns of HU-NiCo₂O₄ and NA-NiCo₂O₄ (Fig. 1b) can be indexed to the (111), (220), (311), (400), (511), (440), and (533) reflections of face-centered cubic-structured NiCo₂O₄ (JCPDS 73-1702). But the crystallinity of HU-NiCo₂O₄ is slightly lower than that of NA-NiCo₂O₄. Fig. 3 shows the morphologies of HU-NiCo₂O₄ and NA-NiCo₂O₄.

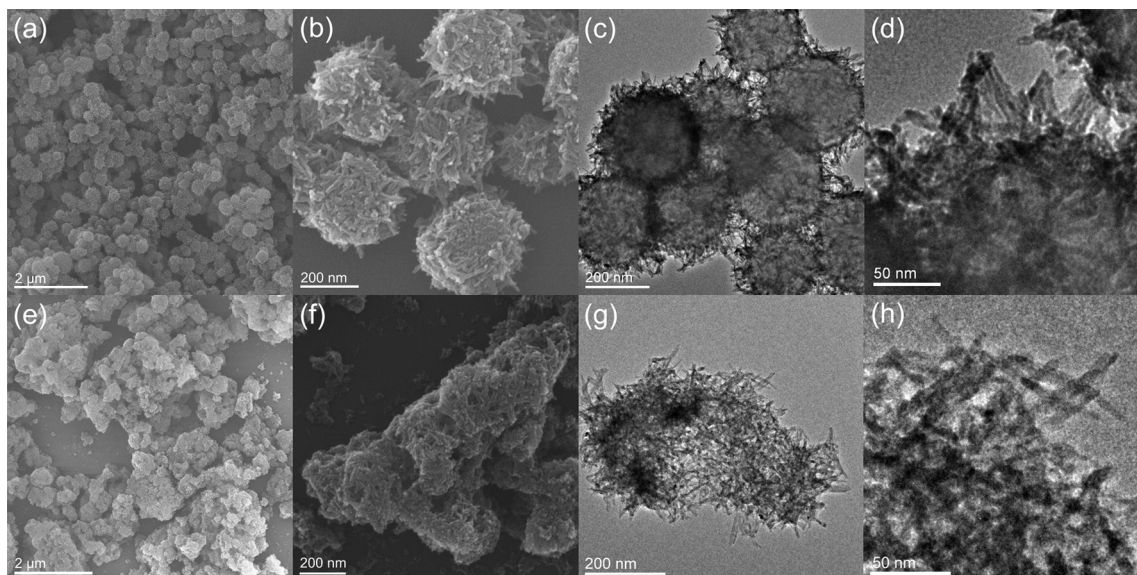


Fig. 2. SEM images of P-HU-NiCo₂O₄ at (a) low and (b) high magnifications. HRTEM images of P-HU-NiCo₂O₄ at (c) low and (d) high magnifications. SEM images of P-NA-NiCo₂O₄ at (e) low and (f) high magnifications. HRTEM images of P-NA-NiCo₂O₄ at (g) low and (h) high magnifications.

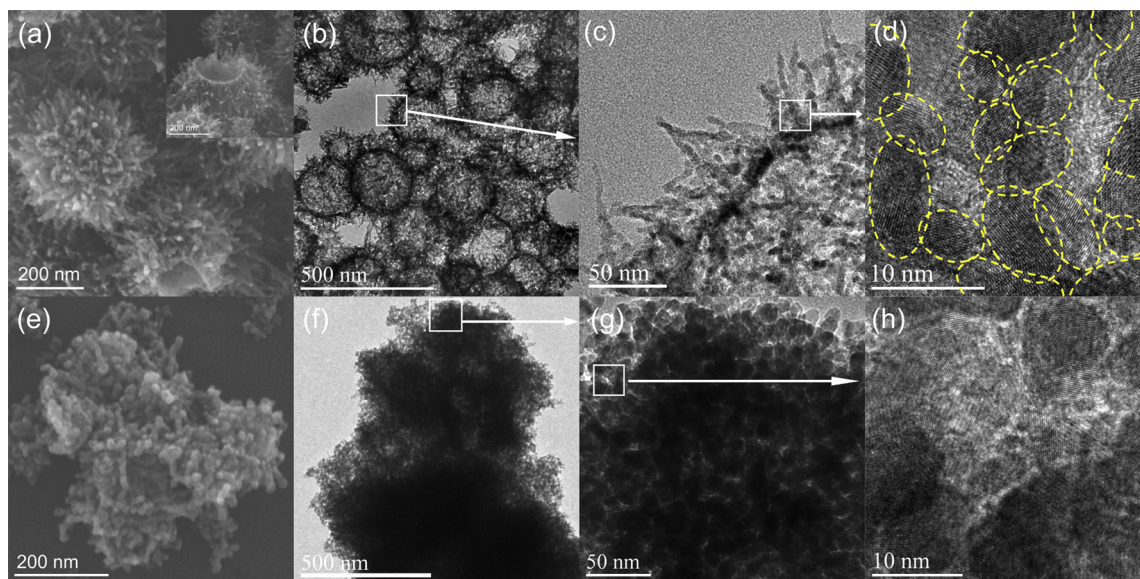


Fig. 3. (a) SEM images of HU-NiCo₂O₄, the inset shows a fractured portion of HU-NiCo₂O₄; (b) HRTEM image of HU-NiCo₂O₄ at low magnifications; (c) a magnification of the white square area in (b); (d) a magnification of the white square area in (c); (e) SEM image of NA-NiCo₂O₄; (f) HRTEM image of NA-NiCo₂O₄ at low magnifications; (g) a magnification of the white square area in (f); (h) a magnification of the white square area in (g).

NiCo₂O₄. HU-NiCo₂O₄ featured a hollow urchin-like morphology, and the diameter of the cavity is estimated at 250 nm (Fig. 3b). HRTEM analysis shows that the hierarchical structure consists of three levels: zero-dimensional nanoparticle with a diameter of about 6 nm (Fig. 3d), one-dimensional chain (Fig. 3c), and three-dimensional hollow urchin-like structure (Fig. 3b), respectively. The thickness of the HU-NiCo₂O₄ shell is estimated at 10 nm (Fig. 3c). In contrast, NA-NiCo₂O₄ features no specific morphology, and consists of randomly and densely aggregated nanoparticles (Fig. 3e–h). The average size of the nanoparticles is about 15 nm. Although there are some pores among the nanoparticles, NA-NiCo₂O₄ is severely agglomerate due to the strong surface energy of nanoparticles.

The fabrication processes of HU-NiCo₂O₄ and NA-NiCo₂O₄ are schematically depicted in Fig. 4. As shown in Fig. 4a, Ni²⁺ and Co²⁺ adsorb on the surface of sulfonated-PS particles upon mixing sulfonated-PS particles with a solution of Ni(NO₃)₂ and Co(NO₃)₂. Subsequent slow addition of Na₂CO₃ produces urchin-like P-HU-

NiCo₂O₄. During calcination in air, both template (sulfonated-PS particles) removal occurs in addition to the reaction shown in Eq. (4). As phase structure transformation and release of gaseous CO₂ and H₂O proceed, the short nanofibers shrink to form a one-dimensional nanochain structure and abundant pores on the shell are formed (Fig. 3c). [19,21,31] Finally, HU-NiCo₂O₄ with a hierarchical hollow urchin-like structure is obtained. The porous shells enable both the outer and inner surfaces of the catalyst to come into contact with the reactants [25] and shorten diffusion length paths of the evolved gas [7]. As shown in Fig. 4b, in the absence of the sulfonated-PS particles, to adsorb Ni²⁺ and Co²⁺, the short nanofibers grow randomly. Following calcination, the randomly arranged short nanofibers shrink to form nanoparticles, producing NA-NiCo₂O₄.

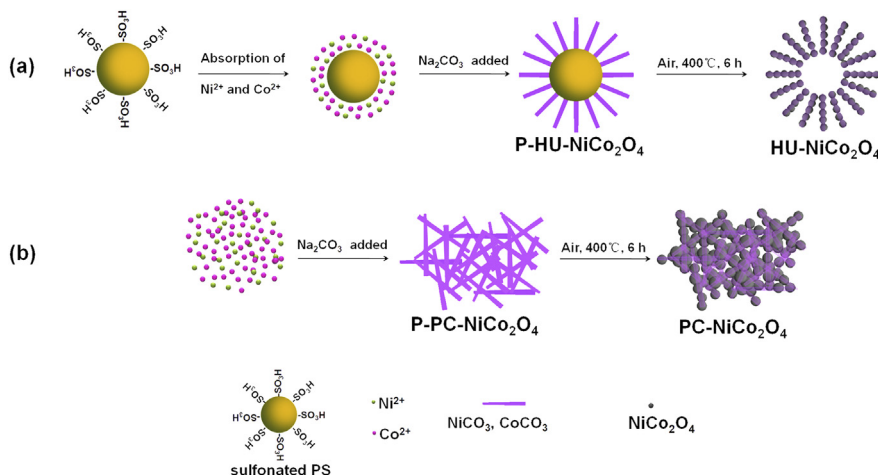
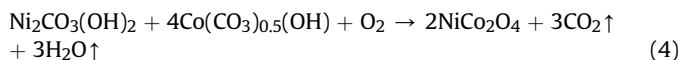


Fig. 4. Schematic illustration of the formation of (a) HU-NiCo₂O₄ and (b) NA-NiCo₂O₄.

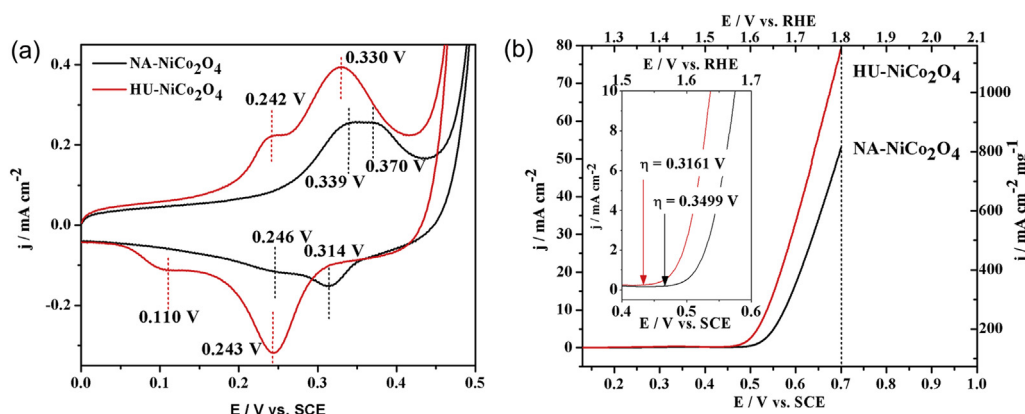


Fig. 5. (a) CV curves of HU-NiCo₂O₄ and NA-NiCo₂O₄ electrodes in O₂-saturated 1 mol L⁻¹ NaOH solution at 1600 rpm at a sweep rate of 5 mV s⁻¹ (b) LSV of the OER for the HU-NiCo₂O₄ and NA-NiCo₂O₄ electrodes in O₂-saturated 1 mol L⁻¹ NaOH solution at 1600 rpm at a sweep rate of 5 mV s⁻¹, the inset is magnification of LSV from 0.4 V to 0.6 V (vs. SCE).

The electrocatalytic activity is usually affected by the electronic configuration and physical property of electrocatalysts. Thus, XPS and BET specific surface areas of HU-NiCo₂O₄ and NA-NiCo₂O₄ were measured. The electronic configurations of Co (Fig. S1a) and Ni (Fig. S1b) for both HU-NiCo₂O₄ and NA-NiCo₂O₄ were almost the same. And HU-NiCo₂O₄ featured a higher BET specific surface area (i.e., 117 m² g⁻¹) when compared with that of NA-NiCo₂O₄ (i.e., 93 m² g⁻¹). The measured roughness factor (*R_f*) values of the HU-NiCo₂O₄ and NA-NiCo₂O₄ electrodes were 84 and 64, respectively, as calculated from the surface double-layer capacitance (Fig. S2). The higher *R_f* value of the HU-NiCo₂O₄ electrode implies that the electrochemical active area is higher than that of the NA-NiCo₂O₄ electrode, which has a lower *R_f* value.

3.2. Catalytic activity of HU-NiCo₂O₄ and NA-NiCo₂O₄ for oxygen evolution

A standard method based on a three-electrode electrochemical cell was used to evaluate the electrocatalytic performance of HU-NiCo₂O₄ and NA-NiCo₂O₄. Fig. 5a shows the CV curves of HU-NiCo₂O₄ and NA-NiCo₂O₄ in 1 mol L⁻¹ NaOH at a scan rate of 5 mV s⁻¹. As observed, there are two anodic peaks and two cathodic peaks for HU-NiCo₂O₄ and NA-NiCo₂O₄ respectively, which means the two kinds of electrocatalysts possess the same electrocatalysis mechanism. The two anodic peaks of HU-NiCo₂O₄ located at 0.242 V and 0.330 V can be assigned to Ni^{II}/Ni^{III} and Ni^{III}, Co^{III}/Ni^{IV}, Co^{IV} transitions, respectively. [37,38] The two cathodic peaks located at 0.243 V and 0.110 V. In contrast, NA-NiCo₂O₄ displayed

different redox peak positions—0.339 V/0.246 V (Ni^{II}/Ni^{III}) and 0.370 V/0.314 V (Ni^{III}, Co^{III}/Ni^{IV}, Co^{IV}). The main influential factors to the different redox peaks position might be the different crystallinity, size of the primary particle and microstructure [36,37,39,40] of HU-NiCo₂O₄ and NA-NiCo₂O₄.

Fig. 5b shows the LSV curves of HU-NiCo₂O₄ and NA-NiCo₂O₄ obtained at a catalyst loading of 0.069 mg cm⁻². The onset overpotential (η_{onset}) of HU-NiCo₂O₄ is lower than that of NA-NiCo₂O₄ by 33.8 mV. Other important electrocatalytic parameters of the electrodes are listed in Table 1. As seen in Table 1, the electrocatalytic performance of HU-NiCo₂O₄ for OER is higher than that of NA-NiCo₂O₄. The superior performance can be attributed to the hierarchical hollow urchin-like structure of HU-NiCo₂O₄. As discussed earlier, the unique structure features a high BET specific surface area, and enables both the outer and inner surfaces of the catalyst to come into contact with the reactants, all of which are highly beneficial towards improved catalytic processes. [25,32,33,41–44] Although the electrocatalyst loading density of the HU-NiCo₂O₄ and NA-NiCo₂O₄ electrodes is lower when compared with those in the literature reports, [15,16,21,45] the produced *j* (mA cm⁻² mg⁻¹) values of the herein prepared electrodes are significantly higher. This can be attributed to the nanocrystalline characteristic of HU-NiCo₂O₄ and NA-NiCo₂O₄. Catalytic reactions are known to proceed on the surface of materials. Hence, the smaller the size of a catalyst, the higher the rate of use of the catalyst per unit mass of catalyst.

Tafel plots of the HU-NiCo₂O₄ and NA-NiCo₂O₄ electrodes are shown in Fig. 6. Based on the linear fitting of the Tafel plots at low

Table 1
OER electrocatalytic parameters of the prepared NiCo₂O₄ nanomaterials.

Modified electrode	HU-NiCo ₂ O ₄ /XC-72/Nafion/RDE	NA-NiCo ₂ O ₄ /XC-72/Nafion/RDE	NiCo ₂ O ₄ /Ni	NiCo ₂ O ₄ NW/Ti	Ni _x Co _{3-x} O ₄ -1:1 NW ^a /Ni
References	This work	This work	[45]	[15]	[16]
Testing condition	1 mol L ⁻¹ NaOH, 25 °C	1 mol L ⁻¹ NaOH, 25 °C	1 mol L ⁻¹ KOH, 25 °C	1 mol L ⁻¹ NaOH, 25 °C	1 mol L ⁻¹ NaOH, 25 °C
Electrocatalyst loading density (mg cm ⁻²)	0.069	0.069	—	2.7	7.4
Tafel slope <i>b</i> (mV dec ⁻¹)	51.3	52.4	70	59	66
η (mV) at 10 mA cm ⁻²	419.3	457.9	360.3	>400	361.6
<i>j</i> ^b at 1.7 V vs. RHE (mA cm ⁻²)	33.1	16.7	114.8	45.4	>74.0
<i>j</i> ^b at 1.8 V vs. RHE (mA cm ⁻²)	479.7	242.0	—	16.8	>10.0
<i>j</i> ^b at 1.8 V vs. RHE (mA cm ⁻² mg ⁻¹)	79.2	52.9	—	—	—
<i>j</i> ^b at 1.8 V vs. RHE (mA cm ⁻² mg ⁻¹)	1147.8	766.7	—	—	—

^a NW, nanowires array.

^b *j*, current density.

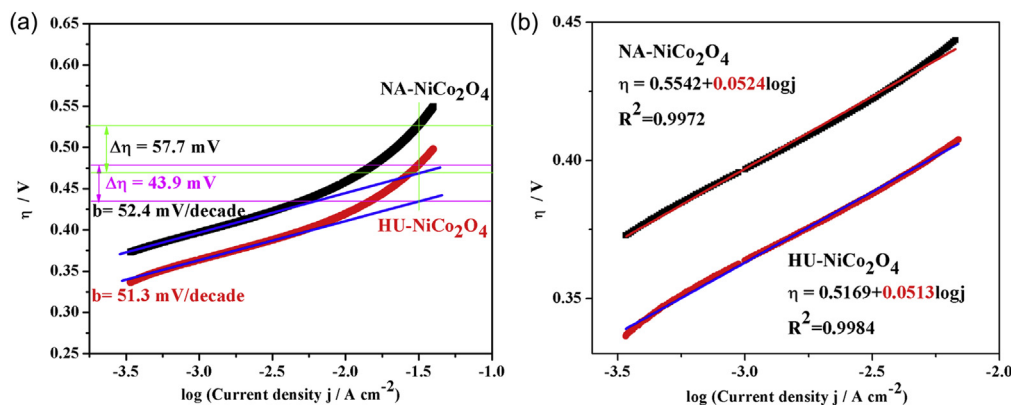


Fig. 6. (a) Tafel plots of HU-NiCo₂O₄ and NA-NiCo₂O₄ electrodes; (b) linear fitting of Tafel plots at low-potential regions.

overpotential (Fig. 6b), the Tafel slope b of HU-NiCo₂O₄ is lower than that of NA-NiCo₂O₄ by 1.1 mV dc^{-1} . As the Fig. 6a shown, at the high overpotential region, polarization curve of NA-NiCo₂O₄ deviates from the linear region larger than that of HU-NiCo₂O₄ by 13.8 mV . The deviation of the polarization curve from the linear region is due to the generation of oxygen gas that decreases the active surface area and drives the electrolyte out of the pores. [15,46] The difference between NA-NiCo₂O₄ and HU-NiCo₂O₄ was attributed to the unique hierarchical architecture of HU-NiCo₂O₄, as illustrated in Fig. 7. The HU-NiCo₂O₄ shell is very thin and comprises abundant pores caused by the phase structure transformation and release of gaseous CO₂ and H₂O during calcination in air, which enable oxygen to escape rapidly from the surface of the catalyst and the electrolyte to effectively infiltrate the catalyst for continuing catalysis processes. [18] In contrast, NA-NiCo₂O₄ features many dense stacking structures that restrict the fast diffusion of oxygen upon generation of large oxygen amounts, which subsequently adheres to the catalyst surface. The residual oxygen decreases the active surface area and drives the electrolyte out of the pores. Thus, polarization curve of NA-NiCo₂O₄ deviates from the linear region larger than that of HU-NiCo₂O₄.

The stability of the HU-NiCo₂O₄ and NA-NiCo₂O₄ electrodes was evaluated and shown in Fig. 8a, b, respectively. After 1200 cycles, the HU-NiCo₂O₄ electrode displays comparable LSV curves with the LSV curve obtained after the first cycle with subtle decrease in the anodic current. In contrast, the NA-NiCo₂O₄ electrode showed a markedly reduced stability. Comparison of the digital photographs of the HU-NiCo₂O₄ (Fig. 8c, e) and NA-NiCo₂O₄ electrodes (Fig. 8d, f) before and after the stability studies revealed that the HU-NiCo₂O₄ electrode featured no changes after the stability test. Contrarily, some parts of the NA-NiCo₂O₄ electrode film had fallen off following the stability test. These observations were consistent with the LSV curves. These results suggest that the microstructure of the electrocatalyst has a significant influence on the stability of the electrode. Owing to the unique structure of HU-NiCo₂O₄, the three-dimensional hollow urchin prevents aggregation of HU-NiCo₂O₄. Additionally, the thin and porous shell connect the cavities to form the well-connected three-dimensional through pore structure, which is beneficial towards efficient oxygen diffusion and consequently highly advantageous towards the high stability of the electrode (Fig. 8g). Conversely, the NA-NiCo₂O₄ electrode film (Fig. 8h) is dense and lacks a well-connected through pore structure. Thus, many paths for oxygen

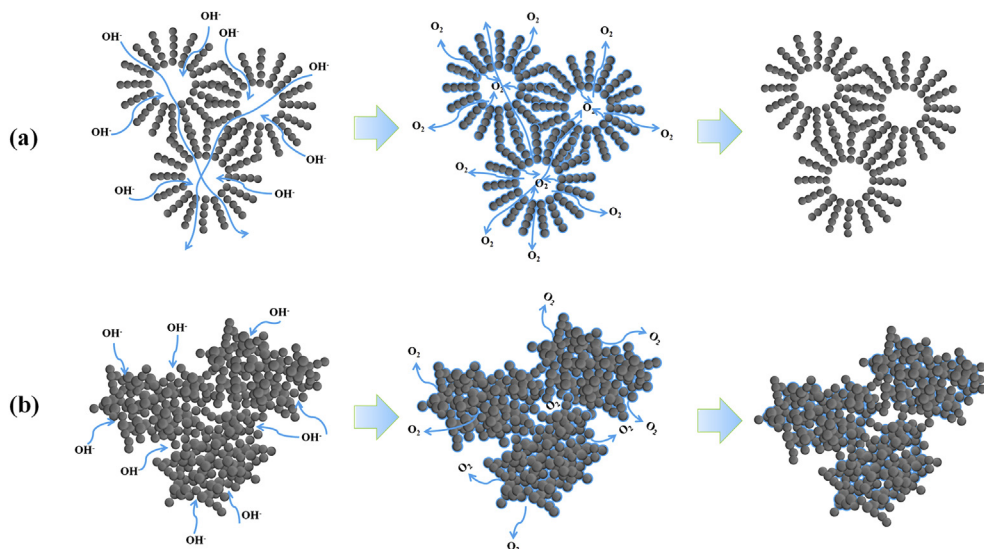


Fig. 7. Schematic illustration of the OER process for (a) HU-NiCo₂O₄ and (b) NA-NiCo₂O₄.

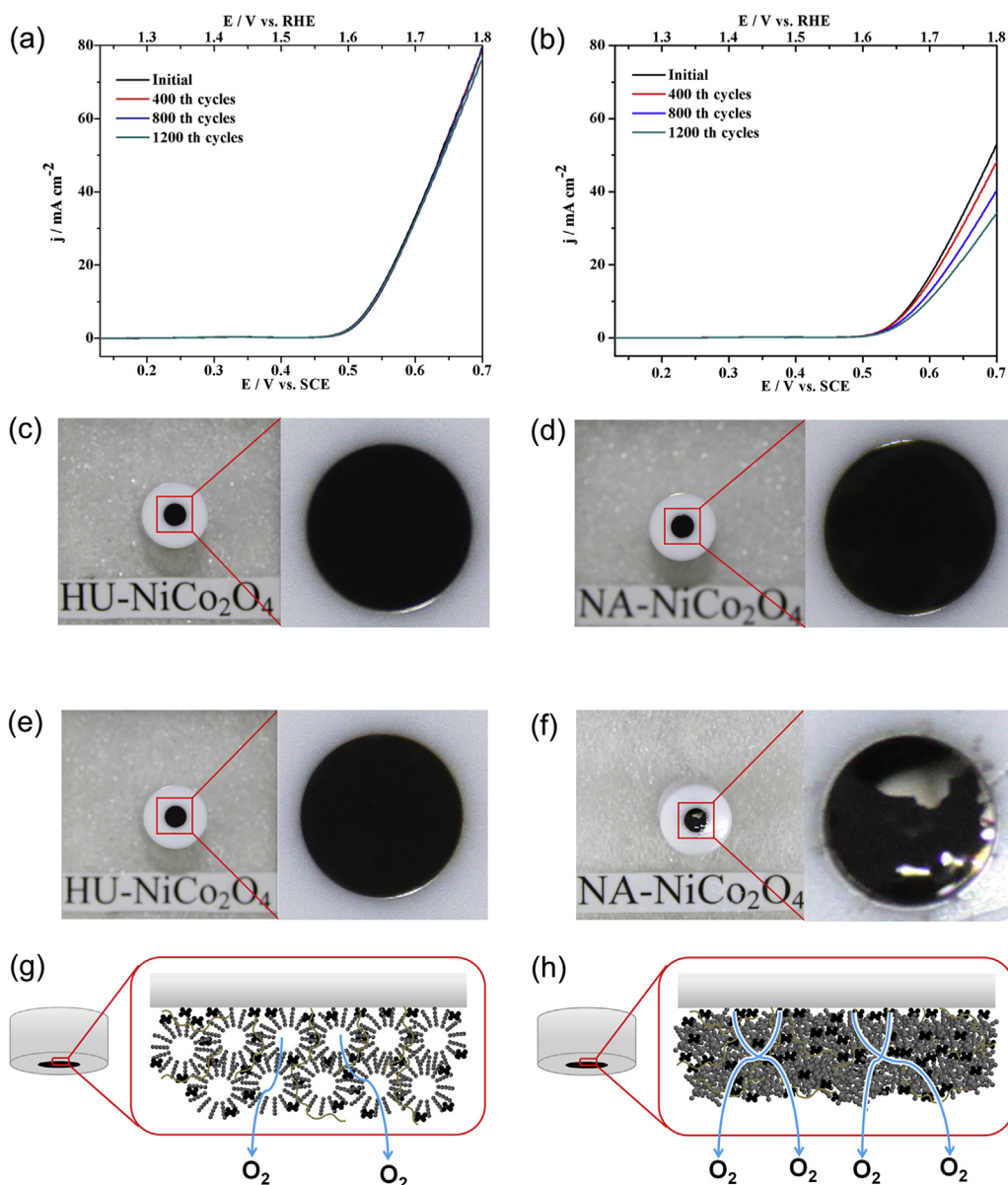


Fig. 8. LSV of the OER for (a) HU-NiCo₂O₄ and (b) NA-NiCo₂O₄ electrodes in O₂-saturated 1 mol L⁻¹ NaOH solution at 1600 rpm at a sweep rate of 5 mV s⁻¹ before cycling, and after 400, 800, and 1200 cycles. Digital photographs of (c) HU-NiCo₂O₄ and (d) NA-NiCo₂O₄ electrodes before the stability test; digital photographs of (e) HU-NiCo₂O₄ and (f) NA-NiCo₂O₄ electrodes after 1200 cycles. Schematic illustration of the O₂ evolution process for (g) HU-NiCo₂O₄ and (h) NA-NiCo₂O₄ electrodes.

diffusion are randomly created during oxygen generation and diffusion, which significantly damage the electrode.

4. Conclusions

We have successfully synthesized HU-NiCo₂O₄ using a hard templating method followed by thermal decomposition. The prepared catalyst shows excellent OER electrocatalytic activity in an alkaline medium. In comparison with NA-NiCo₂O₄, HU-NiCo₂O₄ exhibits lower onset overpotential, significantly smaller deviation of the polarization curve at the high potential region, and higher electrode film stability. The superior electrocatalytic activity and stability of HU-NiCo₂O₄ can be attributed to its unique hierarchical hollow microstructure. The cavities and the pores on the shell are advantageous for fast oxygen diffusion and effective electrolyte infiltration in the catalyst. Moreover, the HU-NiCo₂O₄ electrode with well-connected three-dimensional

through pores has abundant diffusion paths of oxygen, which effectively ensure the high stability of the electrode film. Our studies demonstrate the fabrication of a highly electroactive and low-cost OER electrode based on noble metal-free nanostructured catalysts that are highly applicable in energy conversion technologies.

Acknowledgments

This work was funded by the National Basic Research Program of China (Grant No. 2011CBA00508), the National Natural Science Foundation of China (51272020, 21236003) and the Excellent Ph.D. Thesis Fund of Beijing (YB20101001001). Thesis Fund of Beijing (YB20101001001), the Research Fund for the Doctoral Program of Higher Education of China (20120010110013) and the Program for Changjiang Scholars and Innovative Research Team in University (IRT1205).

Appendix A. Supplementary data

Supplementary data related to this article can be found at <http://dx.doi.org/10.1016/j.jpowsour.2014.06.034>.

References

- [1] M. Gong, Y.G. Li, H.L. Wang, Y.Y. Liang, J.Z. Wu, J.G. Zhou, J. Wang, T. Regier, F. Wei, H.J. Dai, *J. Am. Chem. Soc.* 135 (2013) 8452–8455.
- [2] K. Akihiko, M. Yugo, *Chem. Soc. Rev.* 38 (2009) 253–278.
- [3] F.Y. Cheng, J. Chen, *Chem. Soc. Rev.* 41 (2012) 2172–2192.
- [4] Y.C. Lu, Z.C. Xu, H.A. Gasteiger, S.L. Chen, K. Hamad-Schifferli, Y. Shao-Horn, *J. Am. Chem. Soc.* 132 (2010) 12170–12171.
- [5] Y.M. Lee, J. Suntivich, K.J. May, E.E. Perry, Y. Shao-Horn, *J. Phys. Chem. Lett.* 3 (2012) 399–404.
- [6] W.H. Lee, H. Kim, *Catal. Comm.* 12 (2011) 408–411.
- [7] W. Hu, Y.Q. Wang, X.H. Hu, Y.Q. Zhou, S.L. Chen, *J. Mater. Chem.* 22 (2012) 6010–6016.
- [8] M.C. Chuang, J.A. Ho, *RSC Adv.* 2 (2012) 4092–4096.
- [9] K. Kadakia, M.K. Datta, P.H. Jampani, S.K. Park, P.N. Kumta, *J. Power Sources* 222 (2013) 313–317.
- [10] J. Suntivich, K.J. May, H.A. Gasteiger, J.B. Goodenough, S.H. Yang, *Science* 334 (2011) 1383–1385.
- [11] C. Jin, X. Cao, L. Zhang, C. Zhang, R. Yang, *J. Power Sources* 241 (2013) 225–230.
- [12] M.R. Gao, Y.F. Xu, J. Jiang, Y.R. Zheng, S.H. Yu, *J. Am. Chem. Soc.* 134 (2012) 2930–2933.
- [13] J. Landon, E. Demeter, N. İnoğlu, C. Keturakis, I.E. Wachs, R. Vasić, A.I. Frenkel, J.R. Kitchin, *ACS Catal.* 2 (2012) 1793–1801.
- [14] D.K. Bediako, B. Lassalle-Kaiser, Y. Surendranath, J. Yano, V.K. Yachandra, D.G. Nocera, *J. Am. Chem. Soc.* 134 (2012) 6801–6809.
- [15] Y.G. Li, P. Hasin, Y.Y. Wu, *Adv. Mater.* 22 (2010) 1926–1929.
- [16] B.G. Lu, D.X. Cao, P. Wang, G.L. Wang, Y.Y. Gao, *Int. J. Hydrogen Energy* 36 (2011) 72–78.
- [17] W. Bian, Z. Yang, P. Strasser, R. Yang, *J. Power Sources* 250 (2014) 196–203.
- [18] H.C. Chien, W.Y. Cheng, Y.H. Wang, T.Y. Wei, S.Y. Lu, *J. Mater. Chem.* 21 (2011) 18180–18182.
- [19] B. Cui, H. Lin, J.B. Li, X. Li, J. Yang, J. Tao, *Adv. Funct. Mater.* 18 (2008) 1440–1447.
- [20] B. Sun, J.Q. Zhang, P. Munroe, H.J. Ahn, G.X. Wang, *Electrochem. Comm.* 31 (2013) 88–91.
- [21] D.U. Lee, B.J. Kim, Z.W. Chen, *J. Mater. Chem. A* 1 (2013) 4754–4762.
- [22] Y. Zhang, B. Cui, Z.T. Qin, H. Lin, J.B. Li, *Nanoscale* 5 (2013) 6826–6833.
- [23] S.H. Ahn, S.J. Hwang, S.J. Yoo, I. Choi, H.J. Kim, J.H. Jang, S.W. Nam, T.H. Lim, T. Lim, S.K. Kim, J.J. Kim, *J. Mater. Chem.* 22 (2012) 15153–15159.
- [24] G.J. Du, X.G. Liu, Y. Zong, T.S.A. Hor, A.S. Yu, Z.L. Liu, *Nanoscale* 5 (2013) 4657–4661.
- [25] H.P. Liang, H.M. Zhang, J.S. Hu, Y.G. Guo, L.J. Wan, C.L. Bai, *Angew. Chem. Int. Ed.* 43 (2004) 1540–1543.
- [26] A.M. Cao, J.S. Hu, H.P. Liang, L.J. Wan, *Angew. Chem. Int. Ed.* 44 (2005) 4391–4395.
- [27] J.B. Fei, Y. Cui, X.H. Yan, W. Qi, Y. Yang, K.W. Wang, Q. He, J.B. Li, *Adv. Mater.* 20 (2008) 452–456.
- [28] G.B. Sun, B.X. Dong, M.H. Cao, B.Q. Wei, C.W. Hu, *Chem. Mater.* 23 (2011) 1587–1593.
- [29] A.Q. Pan, H.B. Wu, L. Zhang, X.W. Lou, *Energy Environ. Sci.* 6 (2013) 1476–1479.
- [30] J. Sun, H.M. Liu, X. Chen, D.G. Evans, W.S. Yang, *Nanoscale* 5 (2013) 7564–7571.
- [31] L. Hu, H. Zhong, X.R. Zheng, Y.M. Huang, P. Zhang, Q.W. Chen, *Sci. Rep.* 2 (2012) 986.
- [32] G. Chen, D.G. Xia, Z.R. Nie, Z.Y. Wang, L. Wang, L. Zhang, J.J. Zhang, *Chem. Mater.* 19 (2007) 1840–1844.
- [33] X.W. Lou, L.A. Archer, Z.C. Yang, *Adv. Mater.* 20 (2008) 3987–4019.
- [34] H.L. Cui, H. Chen, R.J. Qu, C.H. Wang, C.N. Ji, C.M. Sun, W.Y. Zhou, M.M. Yu, *J. Appl. Polym. Sci.* 107 (2008) 3909–3916.
- [35] Y.Q. Wu, X.Y. Chen, P.T. Ji, Q.Q. Zhou, *Electrochem. Acta* 56 (2011) 7517–7522.
- [36] Q.F. Wang, B. Liu, X.F. Wang, S.H. Ran, L.M. Wang, D. Chen, G.Z. Shen, *J. Mater. Chem.* 22 (2012) 21647–21653.
- [37] V. Gupta, S. Gupta, N. Miura, *J. Power Sources* 195 (2010) 3757–3760.
- [38] E.B. Castro, C.A. Gervasi, *Int. J. Hydrogen Energy* 25 (2000) 1163–1170.
- [39] R.R. Salunkhe, K.H. Jang, H. Yu, S.H. Yu, T. Ganesh, S.-H. Han, H. Ahn, *J. Alloys Compd.* 509 (2011) 6677–6682.
- [40] H. Wang, X. Wang, *ACS Appl. Mater. Interfaces* 5 (2013) 6255–6260.
- [41] S.B. Yoon, K. Sohn, J.Y. Kim, C.H. Shin, J.S. Yu, T. Hyeon, *Adv. Mater.* 14 (2002) 19–21.
- [42] S.J. Guo, Y.X. Fang, S.J. Dong, E.K. Wang, *J. Phys. Chem. C* 111 (2007) 17104–17109.
- [43] J. Zhao, W.X. Chen, Y.F. Zheng, X. Li, *J. Power Sources* 162 (2006) 168–172.
- [44] G.S. Chai, S.B. Yoon, J.H. Kim, J.S. Yu, *Chem. Comm.* 0 (2004) 2766–2767.
- [45] B. Chi, J.B. Li, Y.S. Han, Y.J. Chen, *Int. J. Hydrogen Energy* 29 (2004) 605–610.
- [46] S.M. Jasem, A.C.C. Tseung, *J. Electrochem. Soc.* 126 (1979) 1353–1360.